Journal of Materials Chemistry A

PAPER

View Article Online
View Journal | View Issue



Cite this: J. Mater. Chem. A, 2015, 3, 5617

# Rational design of three-dimensional nitrogen-doped carbon nanoleaf networks for high-performance oxygen reduction†

Liang Chen,[a] Chenyu Xu,[b] Ran Du,[c] Yueyuan Mao,[a] Cheng Xue,[a] Liming Chen,[a] Liangti Qu,[b] Jin Zhang[c] and Tao Yi*[a]

The application of conventional nanostructure carbon-based materials (such as graphene and carbon nanotubes (CNTs)) as catalysts for the oxygen reduction reaction always suffers from inferior conductivity and low surface area because both graphene and CNTs easily aggregate to form networks with many boundaries. Here, to solve those problems, we have rationally developed "carbon nanoleaf" networks for the oxygen reduction reaction of fuel cells. The "carbon nanoleaf" networks are constructed as aerogels with nitrogen-doped CNTs bridged with graphene nanoribbons (GNRs) by using CNTs as a single precursor. In these carbon nanoleaves, large amounts of unzipped nanoscale GNRs tightly attach to the intact inner walls of the CNTs and thus allow intrinsically good electrical contact. Self-assembly of the carbon nanoleaves into three-dimensional porous aerogel networks with large surface areas guarantees the ultrafast and sufficient mass transfer in the catalytic process. Moreover, the "carbon nanoleaf" networks restrain the aggregation of adjacent CNTs or GNRs, which is inevitable in other 3D CNT and/or graphene nanosheet/GNR networks, to reduce the possibility of the formation of boundaries. Accordingly, the prepared 3D carbon nanoleaf architectures possess a large surface area (380–497 $m^2$ $g^{-1}$) and an excellent conductivity (up to 112 S $m^{-1}$), much higher than those of other reported 3D carbon-based architectures. The "carbon nanoleaf" networks can thus act as newly developed oxygen reduction reaction electrocatalysts with a positive onset potential, ultra-low hydrogen peroxide production and excellent durability that are comparable to or better than those of commercial Pt/C catalysts both in alkaline and acidic solutions.

Received 9th December 2014
Accepted 27th January 2015

DOI: 10.1039/c4ta06764a

www.rsc.org/MaterialsA



## Introduction

With the increasing consumption of energy and approaching depletion of traditional fossil fuels, there is a strong need for new forms of energy. Fuel cells with high energy and power density have been widely considered as green and efficient alternative energy sources and have gradually gained significant attention. Efficient catalysts for the cathodic oxygen reduction reaction (ORR) play a crucial role in the development of fuel cell technology.[1] Pt nanoparticles supported on carbon black (Pt/C) have long been the most active catalyst for ORR. However, their high cost, sluggish ORR process, susceptibility to methanol crossover and limited stability have hampered their further industrial application.[2] Therefore, alternative ORR catalysts with high catalytic activity and selectivity, excellent durability and low cost are highly desirable. To date, tremendous efforts have been devoted to searching for substitutes for platinum-based catalysts.[3–5] In this field, metal-free nitrogen-doped carbon nanomaterials as alternatives to Pt-based catalysts for ORR have become an important research field in recent years due to their low cost, high electrocatalytic activity, good durability and environmental friendliness.[3] Among them, carbon nanotube (CNT)- and graphene nanosheet (GN)-based materials outperform many of their counterparts due to their unique features, including high thermal conductivity, large electron mobility, large surface area and excellent stability.[6,7] Moreover, the incorporation of heteroatoms within the CNT or GN lattice can effectively modulate the electronic energy gap and surface properties of the catalysts, leading to a significant enhancement in the ORR performance, which has been proven by both theoretical calculations and detailed experiments.[8–15] However, it is regrettable that CNTs and GNs easily aggregate to form

[a]Department of Chemistry and Concerted Innovation Center of Chemistry for Energy Materials, Fudan University, 220 Handan Road, Shanghai 200433, China. E-mail: yitao@fudan.edu.cn

[b]Key Laboratory of Cluster Science, Ministry of Education of China, Beijing Key Laboratory of Photoelectronic/Electro-photonic Conversion Materials, Department of Chemistry, School of Science, Beijing Institute of Technology, Beijing 100081, China

[c]Center for Nanochemistry, Beijing National Laboratory for Molecular Sciences, Key Laboratory for the Physics and Chemistry of Nanodevices, State Key Laboratory for Structural, Chemistry of Unstable and Stable Species, College of Chemistry and Molecular Engineering, Peking University, Beijing, 100871, P. R. China

† Electronic supplementary information (ESI) available: The experimental details, additional figures and tables as described in the text. See DOI: 10.1039/c4ta06764a

congeries with many boundaries,[16] which significantly hinders the electron transfer and reduces the electroactive surface area, resulting in a much lower efficiency of the materials than expected.

It is well known that an effective catalyst for a catalytic reaction (such as ORR) should have a combination of several attributes: (1) excellent conductivity (favorable to electron transfer); (2) large specific surface area (favorable to mass transfer); (3) good selectivity (immune to cross effects); and (4) superior stability. Previously reported carbon-based catalysts meet conditions (3) and (4) but often suffer from low conductivity and limited surface area.[3] In our recent work, a versatile nitrogen-doped graphene nanoribbon (GNR) aerogel (NGNRs-A), which showed promising performance as an ORR catalyst in both alkaline and acidic solutions, was developed for the first time.[17] However, the inferior conductivity and partial aggregation of the GNRs compromised its performance due to the existence of boundaries in the self-assembly process of 3D networks. To overcome these drawbacks and to acquire higher performance catalysts for fuel cells, a promising method is the rational design of novel structures to effectively realize charge transport among CNT- or GN-based materials.[18] When it comes to these, nature always gives us inspiration. It is well known that a "leaf" can be simply considered as a hierarchical structure of leaf-blades and leaf-veins coupled with many branches. This exquisite structure ensures that moisture and nutrients are very quickly and adequately delivered to the whole blade through the veins. Inspired by nature, we asked the question of whether CNTs can be simulated into leaf-like structures with structural controllability through simple processing. Very recently, Peng *et al.* reported for the first time CNT bridged GNRs obtained by partial unzipping of the outer walls of the CNTs for application in the field of high-efficiency dye-sensitized solar cells.[16] Although the reported technique is in its infancy and lacks further functionalization research, it provides an efficient strategy to fabricate a leaf-like structure.

One-dimensional (1D) GNRs can be derived from the unzipping of carbon nanotubes, and the completeness of the unzipping process can be controlled by the amount of oxidant.[19] Therefore, CNTs@GNRs with partial unzipping of the outer walls of the CNTs may be simulated as "nanoleaves" at the microscopic level in which the CNTs can be seen as veins and the vimineous GNRs look like blades. The "nanoleaf" is a type of complex bridged structure of CNTs and GNRs in which large amounts of unzipped nanoscale GNRs will tightly attach to the intact inner walls of the nanotubes and thus allow intrinsically good electrical contact. In fact, attempts to combine GNs/GNRs and CNTs have been reported by some groups to study the unique synergistic effect of 1D CNTs and two-dimensional (2D) GNs/1D GNRs. For example, GN–NCNT nanocomposites have been fabricated by Yu's group *via* a one-step hydrothermal process and used as an electrode material for ORR.[20] Similarly, ultralight graphene–CNT hybrid aerogel monoliths with promising performance in water purification have been obtained *via* wet chemistry in Zhang's lab.[21] In both of these works, GNs and CNTs were just artificially mixed and lack a controllable intrinsic structural association (such as interface interaction, 3D self-assembly behavior, *etc.*), which inevitably affects the electron and mass transfer of the carbon networks and thereby compromises the performance of the materials. To the best of our knowledge, methods to assemble hybrids of GNRs and CNTs into macroscopic 3D networks in a controlled manner coupled with hetero-atom doping have not been explored.

In the present work, we developed a simple but efficient method to construct multiporous three-dimensional aerogels based on nitrogen-doped CNTs bridged with GNRs (denoted as N-CNT@GNRs-A) by using CNTs as a single precursor. We called these materials "carbon nanoleaf" cellular networks. An aerogel is a type of ultralight, highly porous nanomaterial with a large surface area.[22,23] The abundance of 3D interconnected mesopores within the aerogels can provide an ideal 3D transport channel for active substances and may thus contribute to the improved mass transfer of materials.[22] Taking into account the unique structural features of the carbon nanoleaf framework, an excellent electrocatalytic performance of our materials was expected due to the ultrafast and sufficient mass transfer and electron transfer within the materials. As a result, the as-prepared 3D carbon nanoleaf architecture possesses a large surface area (380–497 $m^2 g^{-1}$) and an excellent conductivity (up to 112 S $m^{-1}$) and can be used as newly developed ORR electrocatalysts with a quite positive onset potential, ultra-low hydrogen peroxide production and excellent durability, comparable to or better than those of commercial Pt/C catalysts, both in alkaline and acidic solutions. This work thus provides an efficient method for the construction of high-quality carbon-based catalysts.

## Results and discussion

### The synthesis and characterization of the carbon nanoleaves and their analogues

The synthesis of the carbon nanoleaf networks is illustrated in Fig. 1. The details of the synthesis are shown in the ESI.† In the first step, pristine multi-walled CNTs (MWCNTs) were chemically partially unzipped to produce graphene oxide nanoribbons (GONRs) attached to the intact remainder of the CNTs (CNT@GONRs) using an ullage potassium permanganate ($KMnO_4$) ($\leq$400 wt% with respect to the pristine MWCNTs) according to the method reported in a previous study.[19] For comparison, completely unzipped GONRs were also produced using 500 wt% $KMnO_4$.[17] After unzipping, 10 mg $mL^{-1}$ CNT@GONRs in water was sonicated for 30 minutes to form a transparent brown suspension (Fig. S1, ESI†); 5 vol% pyrrole (Py) acting as the N source was added and then sonicated for another 5 minutes to achieve a homogeneous mixture. Hydrothermal treatment of the mixture at 180 °C for 12 h resulted in a mechanically robust monolithic hydrogel. An ultralight carbon nanoleaf framework was obtained by freeze-drying and annealing the aerogel at 1030 °C for 2 h under Ar atmosphere. The formation of a monolithic hydrogel was affected by the amount of $KMnO_4$ and Py monomer. A monolithic hydrogel could not be obtained without addition of Py monomer, indicating that Py plays a vital role in generating such a uniform hydrogel. Py may be adsorbed onto the surface of the

 

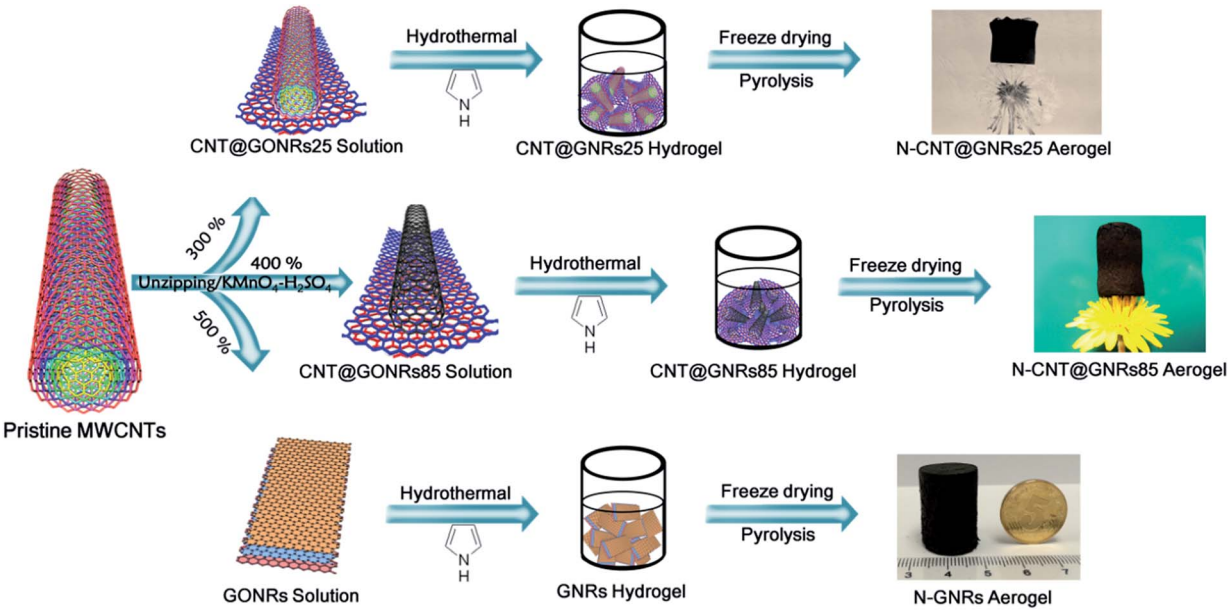


Fig. 1 Illustration of the synthetic route for two kinds of carbon nanoleaf aerogels (N-CNT@GNRs25-A and N-CNT@GNRs85-A) and the reference sample (N-GNRs-A). The last image in each row shows the corresponding aerogel.

CNT@GONRs through hydrogen bonding and π–π interactions during the hydrothermal process and can reduce the concentration of the formed gel significantly, which is consistent with previous literature.[24] If the amount of $KMnO_4$ was less than 300%, the solubility of the as-obtained CNT@GONRs was too poor for acquisition of gels.

X-ray powder diffraction (XRD) was performed to investigate the structure of the partly and completely unzipped CNT@GONRs and the resultant aerogels, as shown in Fig. S2 in the ESI.† The $2\theta$ values located at 25.5° ascribed to pristine CNTs (002) spacing increased with the level of oxidation.[21] When 300 wt% $KMnO_4$ was used to process the pristine CNTs, the resultant CNT@GONRs showed two predominant peaks at 10.6° and 25.4°, with $d$ spacing of 8.3 Å and 3.5 Å, respectively, revealing that the CNTs were partially unzipped to form CNTs bridged with GONR structures. After further increasing the amount of $KMnO_4$ to 400 wt%, the relative intensity of the peak at 10.6° was increased. From the integration of these two peaks, we found that CNT@GONRs contained 25% and 85% GONRs. For simplicity, the samples were denoted as CNT@GONRs25 and CNT@GONRs85, respectively.

After hydrothermal treatment of these precursors and a subsequent high-temperature pyrolysis procedure, the corresponding aerogels and the completely unzipped reference aerogel were obtained, which were denoted as N-CNT@GNRs25-A, N-CNT@GNRs85-A and NGNRs-A. As shown in Fig. 2a, all three samples showed a predominant broad peak at 25.4° in the XRD pattern, indicating that a reduction process occurred and that the GONRs were reduced to GNRs during the hydrothermal and subsequent heat treatment process. Compared to NGNRs-A, the XRD patterns of the two carbon nanoleaf aerogels showed a slight difference in the apparent angle, which may be caused by the two samples retaining intact nanocrystalline CNTs.

To further confirm the partly and completely unzipped CNTs, UV-visible absorption and Raman spectra were also obtained (Fig. S3 and S4, ESI†). Pristine CNTs exhibit a strong absorption peak at 248 nm in the UV-visible spectrum, which can be attributed to the $\pi \rightarrow \pi^*$ transitions of aromatic C–C bonds.[21,25] After unzipping, the resulting N-CNT@GNRs25-A, N-CNT@GNRs85-A and NGNRs-A showed a blue-shift of the absorption from 245 nm to 229 nm with increasing amounts of $KMnO_4$, suggesting a gradual oxidation process (Fig. S3†). Raman spectroscopy was used to determine the structural features of the partly and completely unzipped CNT@GONRs samples and the resultant aerogels. As expected, two predominant peaks at 1348 $cm^{-1}$ and 1582 $cm^{-1}$ were observed for the pristine CNTs samples, corresponding to the D and G bands, respectively. After unzipping, the unzipped samples showed similar D and G bands to those of CNTs, indicating that the structure of CNTs was maintained after the unzipping process. The $I_D/I_G$ intensity ratio is a qualitative measure of the quantity of defects in carbon materials.[26] After treatment with different amounts of $KMnO_4$ (300–500 wt%) for unzipping, the $I_D/I_G$ values of the unzipped samples increased from 0.81 to 0.94 (Fig. S4†), showing an increasing level of disorder with increasing oxidation, consistent with the XRD and UV observations. In the following hydrothermal treatment and high-temperature pyrolysis procedure, the N atoms ascribed to Py in these precursors were *in situ* doped into the GNR skeleton, resulting in the $I_D/I_G$ values of the gels increasing from 1.12 to 1.27 (Fig. 2b), consistent with observations reported previously.[22]

The chemical attributes of the different samples were disclosed by X-ray photoelectron spectroscopy (XPS), as shown in Fig. S5.† In the XPS C 1s spectra of the oxidized nanoribbons, the signals at 284.5 eV and 286.5 eV correspond to C–O and

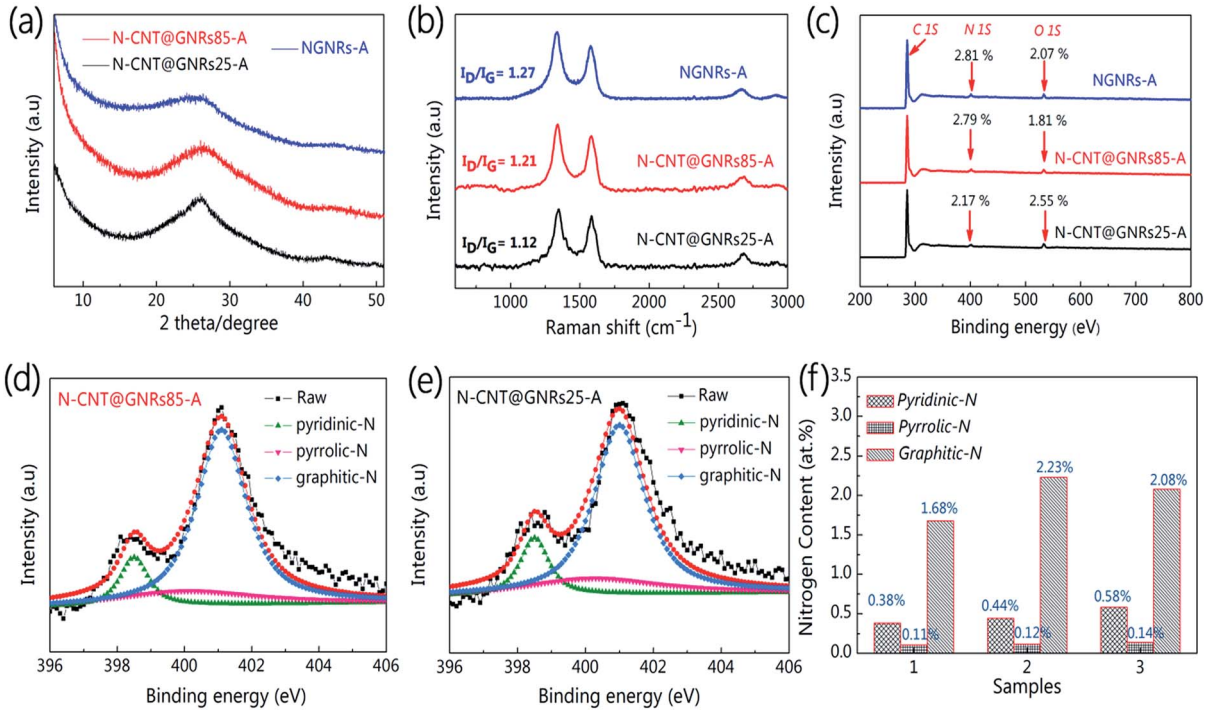


Fig. 2 Typical structure characterizations of the aerogels. (a) XRD patterns and (b) Raman spectra of as-obtained aerogels. (c) XPS survey profiles; and (d and e) high-resolution N 1s peaks of the resulting N-CNT@GNRs25-A and N-CNT@GNRs85-A, respectively. (f) The content of three nitrogen species (pyridinic-N, pyrrolic-N and graphitic-N) in the resultant aerogel samples ((1): N-CNT@GNRs25-A, (2): N-CNT@GNRs85-A, (3): NGNRs-A).

C═O, respectively. The shoulder at 289 eV is assigned to carboxyl groups, revealing that an abundance of oxygen-containing functional groups was generated during the unzipping of the CNTs.[27] The O content of these samples was between 25% and 32%, similar to that of graphene oxide.[21] The XPS spectra of the oxidized nanoribbons showed only C and O peaks, whereas additional N peaks were observed in the assembled aerogels, which confirmed the doping of N atoms within these aerogels.[23] The N contents of the N-CNT@GNRs25-A, N-CNT@GNRs85-A and NGNRs-A were 2.17%, 2.79% and 2.81%, respectively (Fig. 2c). In addition, the XPS-determined O content showed a significant decrease within these aerogels, suggesting that most of the oxygen-containing functional groups were removed during the high-temperature pyrolysis process, which was further confirmed by the high-resolution C 1s spectra of these aerogels. The high-resolution N 1s spectra of the aerogels revealed the presence of pyridinic (398.5 eV), pyrrolic (400.1 eV) and graphitic (401 eV) N atoms (Fig. 2d and e), indicating that the N atoms were doped into these aerogels.[28] When using various oxidized nanoribbons as precursors, the contents of pyridinic, pyrrolic and graphitic N within the corresponding aerogels were slightly different, as seen in Fig. 2f, which can be explained by the distinct unzipping degree and the preservation of some intact internal CNTs.

Besides, we also prepared two analogues (N-GNs/CNT-A and N-GNRs/CNT-A) of the carbon nanoleaves in which GNs or GNRs were mixed with CNTs randomly before the hydrothermal process for comparison (see details in the ESI†). The N-doped contents of N-GNs/CNT-A and N-GNRs/CNT-A were 3.19% and 3.38%, respectively, from the XPS analysis, and the form of the doped N species was all pyridinic, pyrrolic and graphitic N atoms, consistent with that of the carbon nanoleaves (Fig. S6 and S7†).

## The morphological structure of the aerogels

The structure and morphology of the oxidized product (partly and/or completely unraveled CNTs) were monitored using transmission electron microscopy (TEM). As shown in Fig. S8,† after treatment with different amounts of $KMnO_4$, the features of the as-prepared oxidized nanoribbons showed a significant difference. Typically, for CNT@GONRs25, the outer wall of the pristine CNTs exhibited a slight exfoliation to form MWCNTs bridged with a few-layer GONR structure. After increasing the $KMnO_4$ to 400 wt%, most of the outer wall of the pristine CNTs was unzipped to form few-walled CNTs bridged with a multi-layer attached GONR complex. When we used 500 wt% $KMnO_4$, MWCNTs were completely unraveled. The SEM images of the assembled aerogels also confirmed this result (Fig. 3). The carbon nanoleaf aerogels (N-CNT@GNRs25-A and N-CNT@GNRs85-A) exhibited an interconnected, porous structure with hierarchical pores ranging from hundreds of nanometers to tens of micrometers. However, in contrast to the completely unzipped NGNRs-A,[17] the carbon nanoleaves still maintained few-walled CNTs in the 3D network (marked by the arrows in Fig. 3b and f). Similar morphology was also

 

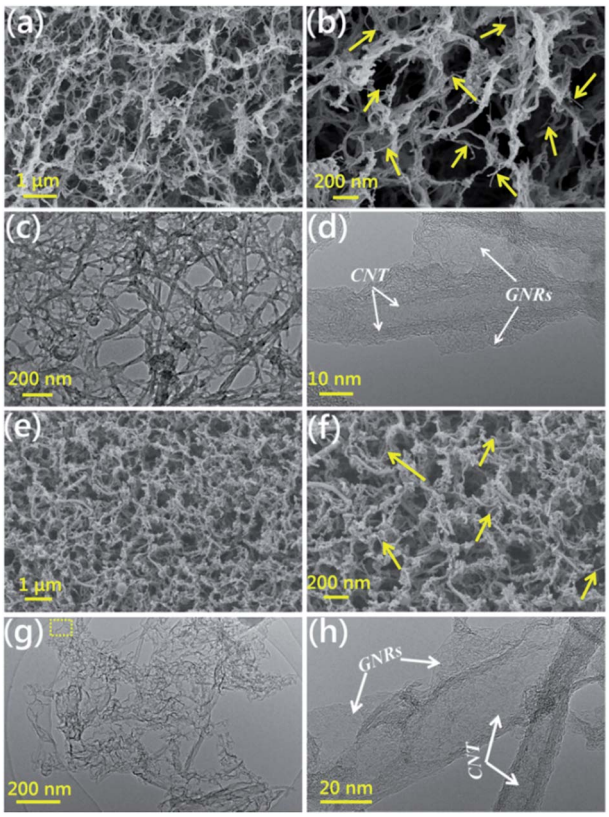


Fig. 3 (a and b) SEM and (c and d) TEM images of as-obtained N-CNT@GNRs25-A. (e and f) SEM and (g and h) TEM images of N-CNT@GNRs85-A. The arrows in (b) and (f) represent the remaining few-walled CNTs in the 3D network.

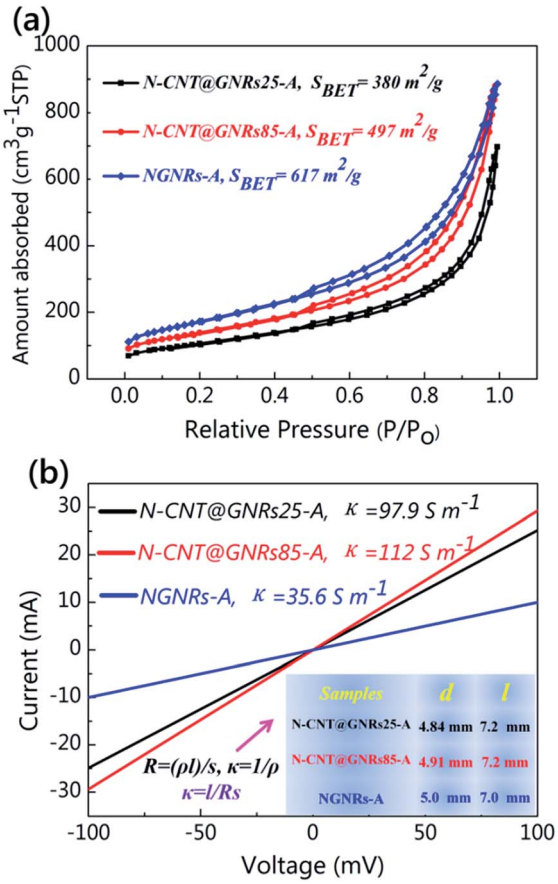


Fig. 4 Typical BET and *I*–*V* test for all samples. (a) Nitrogen sorption isotherms and (b) typical *I*–*V* curves of as-obtained N-CNT@GNRs25-A, N-CNT@GNRs85-A and NGNRs-A. Two-probe method was used to measure electrical conductivities of the samples.

found within aerogels before pyrolysis (Fig. S9†). Moreover, consistent with that of carbon nanoleaf aerogels, the analogues (N-GNs/CNT-A and N-GNRs/CNT-A) also possessed interconnected 3D porous structures as evident from SEM and TEM images (Fig. S10 and S11†).

The porous features and Brunauer–Emmett–Teller (BET) specific surface areas of the carbon nanoleaf frameworks and their analogues were investigated by nitrogen isothermal adsorption/desorption measurements. As shown in Fig. 4a, the adsorption–desorption curves exhibited type-IV isotherms with an $H_3$ hysteresis loop, suggesting an open, wedge-shaped mesoporous structure.[29] The BET specific surface areas for N-CNT@GNRs25-A and N-CNT@GNRs85-A were calculated to be 379 and 497 $m^2\ g^{-1}$, respectively, smaller than that of NGNR-A (617 $m^2\ g^{-1}$) (Table 1), but much higher than those of other carbon-based aerogels.[21,22,24,26,28,30–36] Notably, upon increasing the content of MWCNTs with low specific surface area within the aerogels, the BET surface areas significantly decreased from 617 $m^2\ g^{-1}$ to 379 $m^2\ g^{-1}$. In addition, the BET specific surface areas of the analogues (N-GNs/CNT-A and N-GNRs/CNT-A) were calculated to be 407 and 490 $m^2\ g^{-1}$, respectively (Fig. S12†), close to that of the carbon nanoleaf aerogels. The pore size distributions obtained from the isotherms shown in Fig. S13† indicate a number of mesopores with diameters in the range of 2–3 nm within the aerogels. These mesopores are expected to facilitate the diffusion of reactants in the ORR process. Additionally, the carbon nanoleaf aerogels also possessed good thermal stability; the TGA curves (Fig. S14†) indicated that all of the as-prepared aerogels had a weight loss of less than 9.1 wt% at a temperature up to 800 °C in $N_2$ and can tolerate a high temperature of approximately 400 °C in air.

## The electronic conductivity of the carbon nanoleaves and the analogues

The conductivity of the resulting aerogels was tested by a two-probe method at room temperature. Fig. 4b shows the typical *I*–*V* curves of the carbon nanoleaf frameworks and NGNRs-A. All of the samples present linear *I*–*V* curves, indicating that these samples are conductive.[22] The conductivity for N-CNT@GNRs25-A and N-CNT@GNRs85-A was calculated to be 98 and 112 S $m^{-1}$, respectively (Table 1), much higher than that of NGNRs-A (35.6 S $m^{-1}$) and other 3D carbon-based architectures.[21,22,37–40] The existence of remaining intact CNTs in both N-CNT@GNRs25-A and N-CNT@GNRs85-A may be the main reason for their intrinsically good conductivity. However, the conductivities of N-GNs/CNT-A and N-GNRs/CNT-A were

Table 1 Porous attribute, conductivity, N content (atom %) and the ORR electrocatalytic performance of the N-doped carbon nanoleaf frameworks as well as other comparable catalysts

| Sample[a] | N (%) | BET ($m^2 g^{-1}$) | $\kappa$ (S $m^{-1}$) | Medium | $E_0$ (V) | $E_{1/2}$ (V) | $n$ | Maximum $HO_2^-$ (%) |
|---|---|---|---|---|---|---|---|---|
| N-CNT@GNRs25-A | 2.17 | 379 | 98 | KOH | 0.03 | −0.180 | 3.87–3.94 | 6.45 |
| | | | | $H_2SO_4$ | 0.52 | — | 3.66–3.92 | 11.4 |
| N-CNT@GNRs85-A | 2.79 | 497 | 112 | KOH | 0.04 | −0.178 | 3.89–3.96 | 5.5 |
| | | | | $H_2SO_4$ | 0.58 | — | 3.86–3.94 | 6.7 |
| N-GNRs-A | 2.81 | 617 | 35.6 | KOH | −0.05 | −0.192 | 3.71–3.96 | 14.7 |
| | | | | $H_2SO_4$ | 0.45 | — | 3.77–3.94 | 17.1 |
| N-GNs/CNT-A | 3.19 | 407 | 49.7 | KOH | −0.07 | −0.215 | 3.36–3.94 | 32.1 |
| | | | | $H_2SO_4$ | No | No | No | No |
| N-GNRs/CNT-A | 3.38 | 490 | 63.8 | KOH | −0.04 | −0.195 | 3.77–3.96 | 11.4 |
| | | | | $H_2SO_4$ | 0.49 | — | 3.59–3.96 | 20.5 |

[a] $E_0$: onset potential; $E_{1/2}$: half-wave potential; "—": unknown; "no": no signal in acidic medium.

only 49.7 and 63.8 S $m^{-1}$ (Fig. S15†), respectively, much lower than that of N-CNT@GNRs85-A. The lower conductivity of N-GNs/CNT-A and N-GNRs/CNT-A may be due to the uncontrollable assemblies between the GNs/GNRs and CNTs. That is, the GNs/GNRs were mixed with CNTs randomly; therefore, aggregation easily occurred and formed boundaries within these networks due to the strong π–π interactions between the congeneric GNs/GNRs or the CNTs themselves rather than heterogeneous components.[16] The boundaries compromise their conductivities although these analogues possessed compositions and porous attributes similar to those of N-CNT@GNRs85-A. The superior conductivity of the carbon nanoleaf aerogels ensures that electron transfer is quick and adequate among the 3D networks, facilitating the reduction reaction of oxygen in the ORR process, which we will show below.

### The electrocatalytic behavior of the aerogels

The electrocatalytic activity of the carbon nanoleaf aerogels (N-CNT@GNRs25-A and N-CNT@GNRs85-A) for the ORR was first investigated by cyclic voltammetry (CV) in a $N_2$- and $O_2$-saturated 0.1 M aqueous KOH electrolyte solution at a scan rate of 10 mV $s^{-1}$. For comparison, CV curves of NGNRs-A and their analogue catalysts (N-GNs/CNT-A and N-GNRs/CNT-A) were also obtained. As shown in Fig. 5a and S16a,† featureless voltammetric currents within the potential range of −1.0 V to +0.2 V were observed for all the aerogels in the $N_2$-saturated solution (dotted curve). In contrast, when the electrolyte was saturated with $O_2$, a well-defined cathodic peak centered at approximately −0.13 V, −0.12 V, −0.17 V, −0.21 V and −0.17 V for N-CNT@GNRs25-A, N-CNT@GNRs85-A, NGNRs-A, N-GNs/CNT-A and N-GNRs/CNT-A, respectively, was detected, suggesting pronounced electrocatalytic activity of the carbon nanoleaf aerogels and reference catalysts.[41] To gain further insight into the kinetics of the ORR on the three electrodes, rotating disk electrode (RDE) linear sweep voltammetry was performed in an $O_2$-saturated 0.1 M KOH solution at a scanning rate of 10 mV $s^{-1}$. As shown in Fig. 5b and S16b,† the onset potentials ($E_0$) of N-CNT@GNRs25-A (0.03 V) and N-CNT@GNRs85-A (0.04 V) were much more positive than those of pristine MWCNTs (−0.20 V), pure GNRs (−0.16 V), NGNRs-A (−0.05 V), N-GNs/CNT-A (−0.07 V) and N-GNRs/CNT-A (−0.04 V), as well as of other recently reported heteroatom-doped carbon-based nanomaterials (Tables 1 and S1†).[42–46] The values are similar to that of commercial Pt/C catalyst (approx. 0.05 V), suggesting the excellent electrocatalytic activity of the carbon nanoleaf aerogels. Moreover, the half-wave potentials ($E_{1/2}$) of N-CNT@GNRs85-A ($E_{1/2} = -0.178$ V) and N-CNT@GNRs25-A ($E_{1/2} = -0.180$ V) were also higher than those of NGNRs-A ($E_{1/2} = -0.192$ V), N-GNs/CNT-A ($E_{1/2} = -0.215$ V), N-GNRs/CNT-A ($E_{1/2} = -0.195$ V) and only approximately 54 mV more negative than that of the Pt/C catalyst ($E_{1/2} = -0.124$ V).

The effect of the heating temperature on the catalytic activity of the two kinds of carbon nanoleaf aerogels was also investigated. The aerogels (N-CNT@GNRs25-A and N-CNT@GNRs85-A) carbonized at 1030 °C possessed the highest onset potential and largest cathodic current density (Fig. S17†). For a lower annealing temperature, fewer catalytic active sites can be generated on the carbon matrix, resulting in inferior ORR performance, which is consistent with previous reports.[8] However, if we further increase the annealing temperature, the N-content which is doped into the carbon-based materials will decrease remarkably, thus lowering the ORR activity, which has been proved by previously reports.[47–50]

On the other hand, carbon-based electrocatalysts generally possess sluggish ORR processes and often suffer from poor electron transfer to the adsorbed oxygen molecules, *i.e.*, the two-electron reduction of oxygen may also occur, accompanied by the four-electron reaction, which is less desired due to the low efficiency and the corrosive nature of the resulting hydrogen peroxide.[51] To further confirm the electron transfer number ($n$) and the peroxide yield of the carbon nanoleaf foams during the ORR process, rotating ring-disk electrode (RRDE) analysis was performed, as shown in Fig. 5c and S16c.† The $n$ values obtained from the RRDE curves for N-CNT@GNRs85-A were 3.89–3.96 over the measured potential range (Fig. 5d), similar to those of N-CNT@GNRs25-A (3.87–3.94), NGNRs-A (3.71–3.96), N-GNs/CNT-A (3.36–3.94) and N-GNRs/CNT-A (3.77–3.96) (Fig. S16d†) and approaching that of Pt/C catalysts (~4e), suggesting that all the samples

 

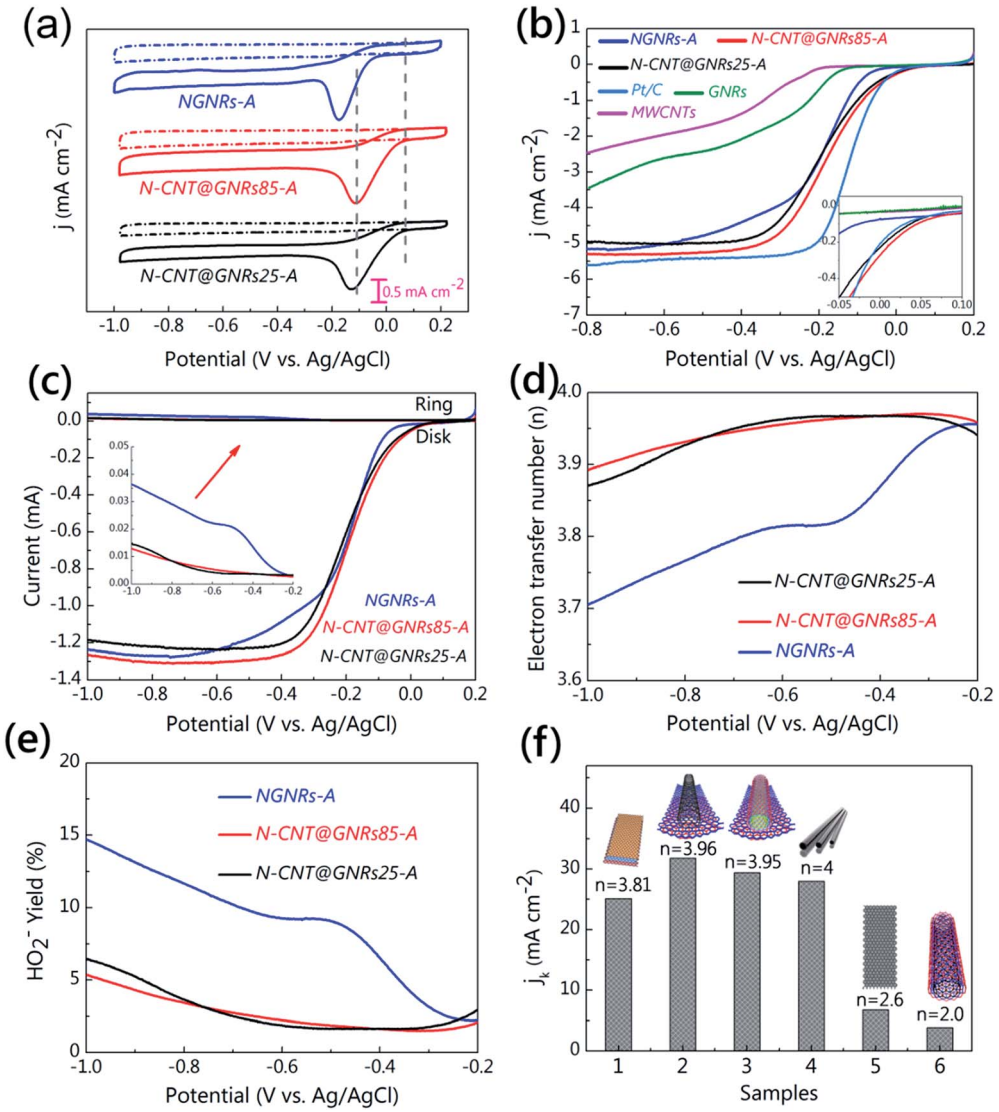


Fig. 5 Electrocatalytic activities of resultant aerogels in alkaline solution. (a) CV curves of as-prepared N-CNT@GNRs25-A, N-CNT@GNRs85-A and NGNRs-A in a $N_2$- and $O_2$-saturated 0.1 M KOH solution at a scanning rate of 10 mV $s^{-1}$. (b) Rotating disk electrode voltammograms of N-CNT@GNRs25-A, N-CNT@GNRs85-A, NGNRs-A, MWCNTs, GNRs and Pt/C in an $O_2$-saturated 0.1 M KOH solution at a scanning rate of 10 mV $s^{-1}$ and a rotation speed of 1600 rpm. (c) Rotating ring-disk electrode curves of N-CNT@GNRs25-A, N-CNT@GNRs85-A and NGNRs-A at 1600 rpm. (d) Electron transfer number (*n*) and (e) peroxide percentage (%) with respect to the total oxygen reduction product of N-CNT@GNRs25-A, N-CNT@GNRs85-A and NGNRs-A. (f) The kinetic limiting current density of different catalysts at potential of −0.6 V with corresponding *n* derived from RRDE curves. Samples: (1) NGNRs-A; (2) N-CNT@GNRs85-A; (3) N-CNT@GNRs25-A; (4) Pt/C; (5) GNRs; (6) MWCNTs. Insets in (f) are model illustrations of the catalysts with various structures. Catalyst loading was 0.08 mg $cm^{-2}$ for all samples.

show mainly a four-electron ORR mechanism, which is consistent with the RDE measurements (Fig. S18 and S19†). Additionally, the measured $H_2O_2$ yield on the N-CNT@GNRs85-A electrode was less than 5.5% at all potentials, decreasing to ~1.5% at −0.3 V (Fig. 5e), which is slightly superior to that of N-CNT@GNRs25-A (2.96–6.45%). Those values are nearly the same as those of the carbon nanotube–graphene complexes reported by Dai's group (<4%)[3] and much lower than those of NGNRs-A (2.22–14.7%), N-GNs/CNT-A (2.9–32.1%), N-GNRs/CNT-A (1.8–11.4%) and most of the graphene-based ORR catalysts reported previously (Table S1†).[20,24,42–54] The relatively lower electron transfer number and higher peroxide percentage of N-GNs/CNT-A and N-GNRs/CNT-A compared to the N-doped carbon nanoleaf catalysts may be caused by their random assemblies in which GNs/GNRs and CNTs cannot maintain good conductive contact, which further confirmed the superiority of the carbon nanoleaf structural design. In addition, the kinetic limiting current densities of N-CNT@GNRs25-A ($J_k$ = 29.4 mA $cm^{-2}$) and N-CNT@GNRs85-A ($J_k$ = 31.8 mA $cm^{-2}$) were much higher than those of pristine MWCNTs ($J_k$ = 3.86 mA $cm^{-2}$), pure GNRs ($J_k$ = 6.8 mA $cm^{-2}$), NGNRs-A ($J_k$ = 25 mA $cm^{-2}$) and even slightly higher than that of commercial Pt/C ($J_k$ = 28.01 mA $cm^{-2}$) catalyst at −0.6 V (Fig. 5f).

It is well known that for better mass transport within a catalyst, both the oxygen diffusivity and access of aqueous

electrolyte should be considered. Therefore, to further assess the advantages of the structural design for mass transfer in the present work, we analysed the Tafel curves of N-CNT@GNRs25-A and N-CNT@GNRs85-A with different catalyst loading density on the RDE. As expected, on increasing the mass loading of catalysts per area, the onset potential of the catalysts shifts to positive ones and the cathodic current density presents a marked increase (Fig. S20†). Moreover, the high ORR activity of CNT@GNRs25-A and N-CNT@GNRs85-A was further supported by the comparative Tafel slope compared to the Pt/C catalyst. In the high overpotential region (<−0.15 V), where the overall ORR rate is dependent on the oxygen diffusion, the Tafel slope values for CNT@GNRs25-A and N-CNT@GNRs85-A are between 165 and 190 mV $dec^{-1}$. This value is very close to that of the commercial Pt/C catalyst (189 mV $dec^{-1}$) (Fig. S21 and S22†), further confirming the smooth diffusion of the reactant in the carbon nanoleaf aerogel and proving its excellent mass-transfer property.[8] Besides, our prepared carbon nanoleaf aerogels are super-hydrophilic (the water contact angle is close to 0°), due to the N-doped nature (Fig. S23†), hence the aqueous electrolyte as well as oxygen molecules can enter into the pores of the aerogels easily and react immediately. Based on the above facts, we believed that the carbon nanoleaf aerogels favour a better mass transfer for the ORR.

In a word, the relatively positive onset potential, half-wave potential and the cathodic current density compared to the other reference samples and NGNRs-A can be attributed to the exquisite structures of the carbon nanoleaves, which ensure efficient mass transfer and electron transfer to the catalytic sites and markedly facilitate ORR diffusion kinetics, in spite of the relatively lower BET surface areas and lower N doping content. The superior catalytic performance of the carbon nanoleaf aerogels toward ORR supports the proposed synergistic effect of 1D CNTs and 1D GNRs derived from their unique bridge structure. All of the results mentioned above support the conclusion that the carbon nanoleaf aerogels are efficient catalysts for ORR in alkaline medium.

Conventional carbon-based materials show low ORR activities in acidic solutions due to the lack of catalytic sites.[3] Only limited research on metal-free graphene-based catalysts has reported pronounced electrocatalytic activity under acidic conditions.[3,55–57] Therefore, rationally designing novel doped carbon-based catalysts with superior catalytic performance in acidic medium is extremely desirable. With this in mind, the electrocatalytic performances of the carbon nanoleaf catalysts toward ORR in an acidic medium were investigated by CV in $O_2$-saturated 0.5 M $H_2SO_4$. Commercial 20 wt% platinum on carbon black (Pt/C) was measured in an acidic medium for comparison (Fig. S24†). As shown in Fig. 6a and S25a,† the ORR onset potential ($E_0$) and peak potential ($E_p$) of the N-CNT@GNRs85-A electrode were 0.58 and 0.38 V, respectively, *vs.* the Ag/AgCl reference electrode, much more positive than those of N-CNT@GNRs25-A ($E_0$ = 0.52 V and $E_P$ = 0.27 V), NGNRs-A ($E_0$ = 0.45 V and $E_P$ = 0.20 V), N-GNRs/CNT-A ($E_0$ = 0.49 V and $E_P$ = 0.26 V) and other heteroatom-doped graphene-based materials under the same conditions.[57] However, due to the poor activity of the N-GNs/CNT-A catalyst, the N-GNs/CNT-A electrode did not show any signal when the electrolyte was saturated with $O_2$ in 0.5 M $H_2SO_4$ (Fig. S26†). The high catalytic activity of N-CNT@GNRs85-A in the acidic medium is facilitated by the strong coupling between CNTs and GNRs. Although the N-CNT@GNRs25-A sample has a similar structure, the relatively lower BET surface area and the lower N doping content compromised its catalytic performance compared to that of N-CNT@GNRs85-A. Similar trends in the ORR activities were also observed in the RRDE measurements. As shown in Fig. 6b and S25b,† N-CNT@GNRs85-A catalyst outperformed the N-CNT@GNRs25-A, NGNRs-A and N-GNRs/CNT-A catalysts in terms of the onset potential. The disk current density of the two carbon nanoleaves was also higher than that of NGNRs-A.

In addition, the percentage of peroxide species with respect to the total oxygen reduction products and the electron reduction number ($n$) calculated from the RRDE curves suggest that reactions for all of the catalysts proceed mainly through the four-electron (4e) pathway in acidic solutions. The $n$ values were 3.86–3.94 for N-CNT@GNRs85-A, 3.77–3.94 for N-CNT@GNRs25-A, 3.66–3.92 for NGNRs-A and 3.59–3.94 for N-GNRs/CNT-A (Fig. 6c and S20c†) at all potentials. The $H_2O_2$ yield was 3–6.7% from −0.2 to 0.4 V for N-CNT@GNRs85-A, much lower than that of N-CNT@GNRs25-A (3–11.4%), NGNRs-A (4.2–17.1%) and N-GNRs/CNT-A (2.5–20.5%) (Fig. 6d and S25c†). The $n$ values obtained from the *K–L* plots based on the RDE measurements (Fig. S25d and S27†) were consistent with the RRDE results.

In light of practical application in fuel cells, fuel molecules (*e.g.*, methanol) may pass through the membrane from anode to cathode and poison the cathode catalyst. The carbon nanoleaf electrodes, NGNRs-A electrode and Pt/C catalyst were thus exposed to methanol to verify possible crossover and poisoning effects. As shown in Fig. 7a, when 3 M methanol was introduced into the electrolyte, the carbon nanoleaves and NGNRs-A electrode showed no noticeable change, indicating high catalytic selectivity against the electro-oxidation of methanol, whereas the Pt/C electrode was rapidly poisoned under the same conditions. These results demonstrated that the carbon nanoleaves possessed a remarkably better tolerance to methanol poisoning than commercial Pt/C. The durability of the carbon nanoleaves with respect to commercial Pt/C and NGNRs-A was assessed through chronoamperometric measurements at −0.4 V in an $O_2$-saturated aqueous solution of 0.1 M KOH at a rotation rate of 1600 rpm. As shown in Fig. 7b, similar to NGNRs-A, the two carbon nanoleaf aerogels both exhibited very slow attenuation after continuous work for 20 000 s, at which time approximately 88% of the relative current was preserved, whereas the Pt/C electrode lost nearly 35% of its initial activity, revealing that the carbon nanoleaf network electrocatalyst is also much more stable than commercial Pt/C in an alkaline medium. This result was also confirmed by accelerated durability tests (Fig. S28†). Obviously, negligible negative shift in the half-wave potential was observed for the two kinds of carbon nanoleaf aerogels (N-CNT@GNRs25-A and N-CNT@GNRs85-A) and N-GNRs-A, while the Pt/C catalyst displayed an inferior durability with obviously cathodic current loss accompanied with negative shift in both the half-wave potential and onset

 

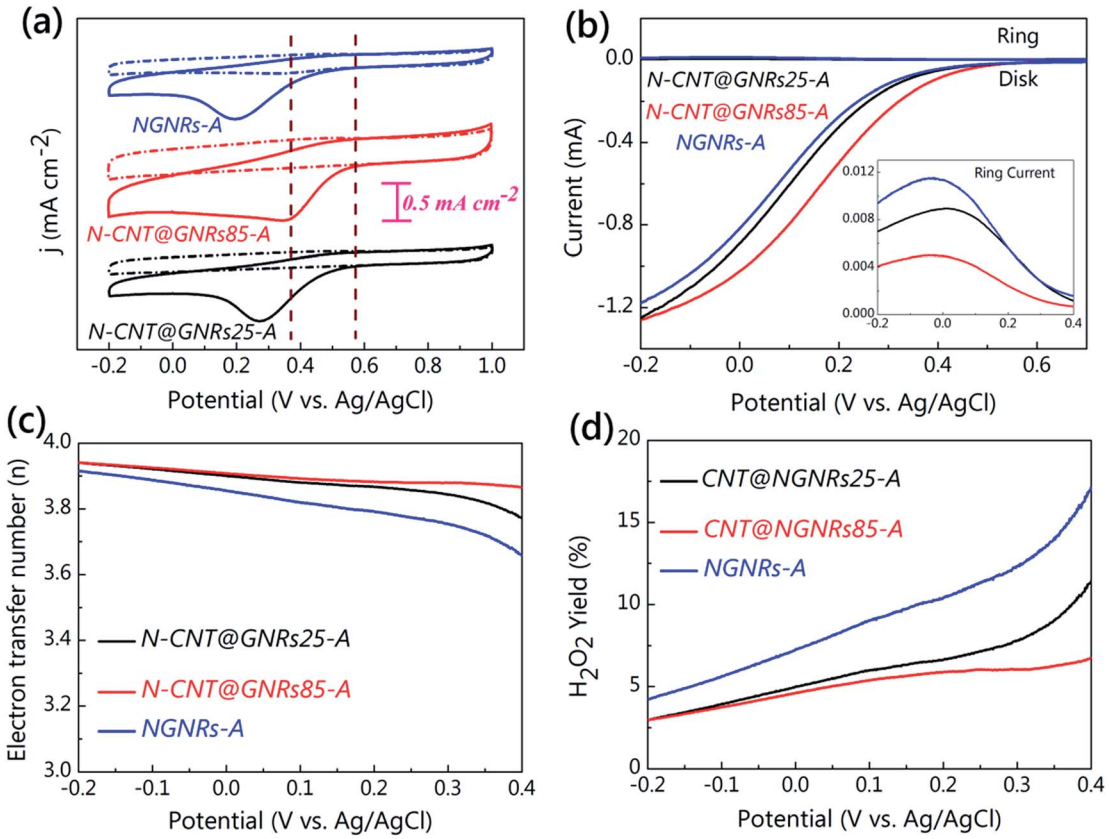


Fig. 6 Electrocatalytic activities of resultant aerogels in acidic solution. (a) CV curves and (b) RRDE voltammograms of as-prepared N-CNT@GNRs25-A, N-CNT@GNRs85-A, NGNRs-A in a $N_2$- and $O_2$-saturated 0.5 M $H_2SO_4$ solution at a scanning rate of 10 mV $s^{-1}$. (c) Electron transfer number (*n*) and (d) peroxide percentage (%) with respect to the total oxygen reduction product of N-CNT@GNRs25-A, N-CNT@GNRs85-A and NGNRs-A. Catalyst loading was 0.08 mg $cm^{-2}$ for all samples.

potential after 3000 potential cycles between 0.2 V and −1.0 V. In addition, N-CNT@GNRs85-A also has a better durability than commercial Pt/C in acidic solutions (Fig. S29†).

To further determine the origin of the excellent ORR performance of the carbon nanoleaf cellular networks, we investigated their structural features to determine the unique synergistic effect of the "carbon nanoleaf" structure on the electron transfer and mass transfer toward ORR. HRTEM confirmed that the carbon nanoleaves consisted of two building blocks (Fig. 8a) in which 1D CNTs were bridged with 1D GNRs. The intact inner walls of the nanotubes lying on the nanoscale GNRs formed a bond structure of CNT@GNRs. The intact CNTs can maintain their good electrical conductivity, and the unzipped GNRs can provide a large specific surface area. Therefore, the electron transfer should be more rapid between CNTs and GNRs than other random CNT and/or GN/GNR 3D networks (Fig. 8b), which was confirmed by the *I–V* tests. In addition, through this ingenious design, we have integrated rigid CNTs and flexible GNRs together, making the N-CNT@GNRs-A monoliths robust enough to retain their porous 3D structure when the pores were filled with liquid, favoring a better mass transfer for the ORR. Compared with their film-structured counterparts, which lack an abundant pore structure, the pores/spaces formed between adjacent carbon nanoleaves enabled fast mass transport throughout the carbon nanoleaves in a 3D model (allowing the mass transport in multiple dimensions and multiple directions) due to the nanoscale pores within the cellular networks (Fig. 8c and d), and, as a result, the performance would be enhanced.[58] Moreover, this unique structure can restrain the aggregation of adjacent CNTs or GNRs, which is inevitable in other 3D CNT and/or GN/GNR networks. When the adjacent CNTs are close to each other, the embedded GNRs can act as spacers to impede their aggregation. When the adjacent GNRs aggregate, the bonded, intact CNTs can also serve as spacers to inhibit the stacking of GNRs. Therefore, this quirky design can reduce the possibility of the formation of boundaries, whereas with conventional CNT and/or GN/GNR 3D networks, the formation of boundaries is unavoidable. Furthermore, the addition of Py monomer not only serves as doped N species which enhance the reactivity and electrocatalytic ability of GNRs but also as a swelling agent to suppress the shrinkage of the gel, resulting in a porous structure of the materials. EDS mapping shows that the doped N species have a homogeneous distribution throughout the carbon nanoleaf cellular networks (Fig. S30†). As a result, the catalytic reaction can be performed within the entire material rather than only in some local regions. All of the results mentioned above support the conclusion that the carbon nanoleaves are efficient catalysts for ORR, both in acidic and alkaline solutions.

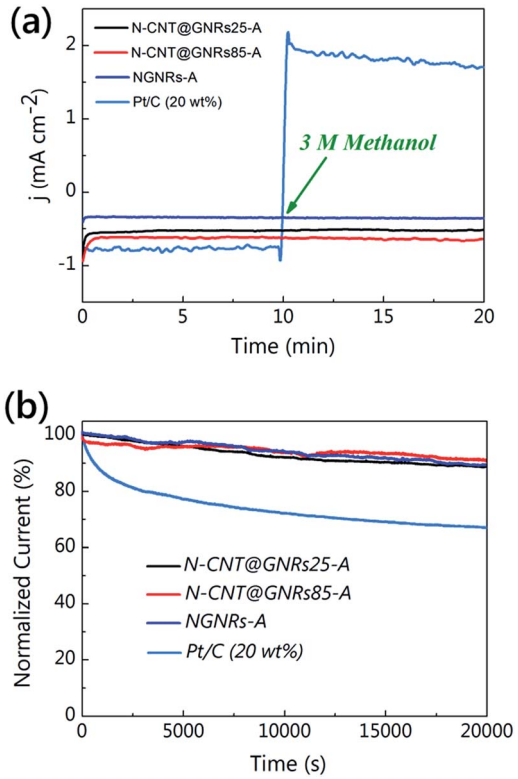


Fig. 7 The stability of resulting aerogels. (a) Methanol crossover effect test of resulting samples and Pt/C catalyst upon addition of 3 M methanol after about 10 min in an $O_2$-saturated 0.1 M KOH solution at −0.4 V. (b) Current–time chronoamperometric response of as-obtained aerogel samples and Pt/C catalysts at −0.4 V in $O_2$-saturated aqueous solution of 0.1 M KOH at a rotation rate of 1600 rpm.

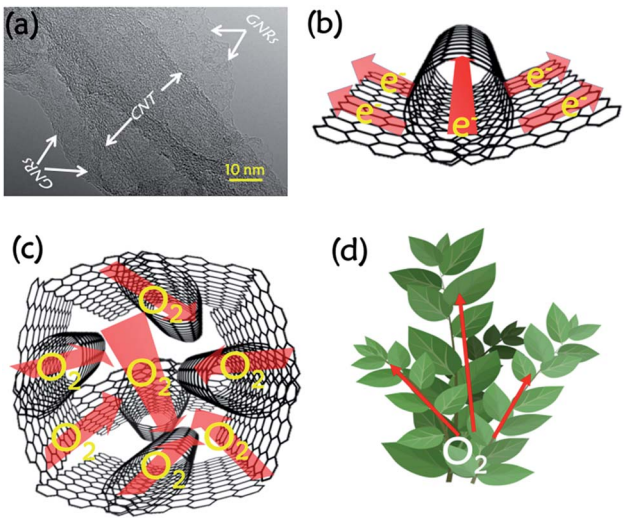


Fig. 8 (a) HRTEM image of as-prepared carbon nanoleaf aerogels, in which GNRs and CNT are labeled. Scheme of (b) the carbon nanoleaf bridged structure (CNT@GNRs) for enhancing electron transfer and of (c) the interpenetrated 3D porous network for facilitating mass transfer (here exemplified with molecular oxygen). (d) Natural pattern for facilitating mass transfer in an actual cluster of leaves.

## Conclusions

In summary, we successfully fabricated a type of carbon nanoleaf framework using MWCNTs as a single precursor. Through this rational design, we acquired an effective method for the hybridization of CNTs and GNRs in a controlled manner. The resulting carbon nanoleaf frameworks possessed low density, large surface area and good conductivity. Based on these characteristics, the resultant carbon nanoleaf frameworks can act as ORR catalysts with superb electrocatalytic activity, excellent tolerance to methanol and superior stability, both in acidic and alkaline solutions. The excellent catalytic properties for ORR can be attributed to the synergistic effect of the N-doped, nanoporous structure, structural integrity, high surface area and good conductivity, which originated from the unique bridged structure of the CNTs and GNRs, ensuring that electron transfer and mass transfer are more rapid and complete within CNT@GNRs than other random CNT and/or GN/GNR 3D networks. The catalyst synthesis strategy we described here exploits novel carbon-based structures and could represent a general approach to developing other 3D carbon-based monolithic materials for various applications, such as supercapacitors, batteries and oxygen sensors.

## Acknowledgements

The authors are grateful for the financial support of the National Basic Research Program of China (2013CB733700), the China National Funds for Distinguished Young Scientists (21125104), National Natural Science Foundation of China (51373039), Specialized Research Fund for the Doctoral Program of Higher Education (20120071130008), Program for Innovative Research Team in University (IRT1117), and Shanghai Leading Academic Discipline Project (B108).

## Notes and references

1 B. C. Steele and A. Heinzel, *Nature*, 2001, **414**, 345–352.
2 A. Morozan, B. Jousselme and S. Palacin, *Energy Environ. Sci.*, 2011, **4**, 1238–1254.
3 Y. Li, W. Zhou, H. L. Wang, L. M. Xie, Y. Y. Liang, F. Wei, J. C. Idrobo, S. J. Pennycook and H. J. Dai, *Nat. Nanotechnol.*, 2012, **7**, 394–400.
4 Y. Y. Liang, Y. G. Li, H. L. Wang, J. G. Zhou, J. Wang, T. Regier and H. J. Dai, *Nat. Mater.*, 2011, **10**, 780–786.
5 K. Gong, F. Du, Z. Xia, M. Durstock and L. M. Dai, *Science*, 2009, **323**, 760–764.
6 S. Iijima, *Nature*, 1991, **354**, 56–58.
7 A. K. Geim and K. S. Novoselov, *Nat. Mater.*, 2007, **6**, 183–191.
8 W. He, C. Jiang, J. Wang and L. Lu, *Angew. Chem., Int. Ed.*, 2014, **53**, 9503–9507.
9 J. D. Wiggins-Camacho and K. J. Stenvenson, *J. Phys. Chem. C*, 2011, **115**, 20002–20010.
10 C. V. Rao and Y. Ishikawa, *J. Phys. Chem. C*, 2012, **116**, 4340–4346.
11 J. D. Wiggins-Camacho and K. J. Stenvenson, *J. Phys. Chem. C*, 2009, **113**, 19082–19090.

12 Z. Chen, D. Higgins, A. Yu, L. Zhang and J. Zhang, *Energy Environ. Sci.*, 2011, **4**, 3167–3192.
13 C. V. Rao, C. R. Cabrera and Y. Ishikawa, *J. Phys. Chem. Lett.*, 2010, **1**, 2622–2627.
14 H. Kim, K. Lee, S. I. Woo and Y. Jung, *Phys. Chem. Chem. Phys.*, 2011, **13**, 17505–17510.
15 G. Tuci, C. Zafferoni, P. D'Ambrosio, S. Caporali, M. Ceppatelli, A. Rossin, T. Tsoufis, M. Innocenti and G. Giambastiani, *ACS Catal.*, 2013, **3**, 2108–2111.
16 Z. Yang, M. K. Liu, C. Zhang, W. W. Tjiu, T. X. Liu and H. S. Peng, *Angew. Chem., Int. Ed.*, 2013, **52**, 3996–3999.
17 L. Chen, R. Du, J. Zhu, Y. Mao, C. Xue, N. Zhang, Y. Hou, J. Zhang and T. Yi, *Small*, 2014, **10**, DOI: 10.1002/smll.201402472.
18 C. Cui, W. Z. Qian, Y. T. Yu, C. Y. Kong, B. Yu, L. Xiang and F. Wei, *J. Am. Chem. Soc.*, 2014, **136**, 2256–2259.
19 D. V. Kosynkin, A. L. Higginbotham, A. Sinitskii, J. R. Lomeda, A. Dimiev, B. K. Price and J. M. Tour, *Nature*, 2009, **458**, 872–876.
20 P. Chen, T. Y. Xiao, Y. H. Qian, S. S. Li and S. H. Yu, *Adv. Mater.*, 2013, **25**, 3192–3196.
21 Z. Sui, Q. Meng, X. Zhang, R. Ma and B. Cao, *J. Mater. Chem.*, 2012, **22**, 8767–8771.
22 L. Chen, B. Wei, X. Zhang and C. Li, *Small*, 2013, **9**, 2331–2340.
23 N. Gaponik, A. K. Herrmann and A. Eychmüller, *J. Phys. Chem. Lett.*, 2012, **3**, 8–17.
24 Y. Zhao, C. G. Hu, Y. Hu, H. H. Cheng, G. Q. Shi and L. T. Qu, *Angew. Chem., Int. Ed.*, 2012, **51**, 11371–11375.
25 Y. Xu, L. Sheng, C. Li and G. Q. Shi, *ACS Nano*, 2010, **4**, 4324–4330.
26 Z. S. Wu, A. Winter, L. Chen, Y. Sun, A. Turchanin, X. L. Feng and K. Müllen, *Adv. Mater.*, 2012, **24**, 5130–5135.
27 Y. Li, Y. Zhao, H. H. Cheng, Y. Hu, G. Q. Shi, L. M. Dai and L. T. Qu, *J. Am. Chem. Soc.*, 2012, **134**, 15–18.
28 Y. Xue, J. Liu, H. Chen, R. G. Wang, D. Q. Li, J. Qu and L. M. Dai, *Angew. Chem., Int. Ed.*, 2012, **51**, 12124–12127.
29 L. Chen, X. D. Zhang, H. W. Liang, M. G. Kong, Q. F. Guan, Z. Y. Wu and S. H. Yu, *ACS Nano*, 2012, **6**, 7092–7102.
30 H. Sun, Z. Xu and C. Gao, *Adv. Mater.*, 2013, **25**, 2554–2560.
31 X. Cao, Z. Yin and H. Zhang, *Energy Environ. Sci.*, 2014, **7**, 1850–1865.
32 Y. Gong, S. B. Yang, Z. Liu, L. L. Ma, R. Vajtai and P. M. Ajayan, *Adv. Mater.*, 2013, **25**, 3979–3984.
33 Q. Peng, Y. Li, X. He, X. Gui, Y. Shang, C. Wang, C. Wang, W. Zhao, S. Du, E. Shi, P. Li, D. H. Wu and A. Y. Cao, *Adv. Mater.*, 2014, **26**, 3241–3247.
34 H. Hu, Z. Zhao, W. Wan, Y. Gogotsi and J. Qiu, *Adv. Mater.*, 2013, **25**, 2219–2223.
35 Y. Xu, Z. Lin, X. Huang, Y. Wang, Y. Huang and X. F. Duan, *ACS Nano*, 2013, **6**, 656–661.
36 S. Nardecchia, D. Carriazo, M. L. Ferrer, M. C. Gutiérrez and F. Monte, *Chem. Soc. Rev.*, 2013, **42**, 794–830.
37 Z. Y. Wu, C. Li, H. W. Liang, J. F. Chen and S. H. Yu, *Angew. Chem., Int. Ed.*, 2013, **52**, 2925–2929.
38 G. L. Tian, M. Q. Zhao, D. S. Yu, X. Y. Kong, J. Q. Huang, Q. Zhang and F. Wei, *Small*, 2014, **10**, 2251–2259.
39 L. Zhang, F. Zhang, X. Yang, G. Long, Y. Wu, T. Zhang, K. Leng, Y. Huang, Y. Ma, A. Yu and Y. S. Chen, *Sci. Rep.*, 2013, **3**, 1408–1417.
40 X. Zhang, Z. Y. Sui, B. Xu, S. F. Yue, Y. J. Luo, W. Zhan and B. Liu, *J. Mater. Chem.*, 2011, **21**, 6494–6497.
41 Y. Jiao, Y. Zheng, M. Jaroniec and S. Z. Qiao, *J. Am. Chem. Soc.*, 2014, **136**, 4394–4403.
42 L. T. Qu, Y. Liu, J. B. Beak and L. M. Dai, *ACS Nano*, 2010, **4**, 1321–1326.
43 Z. H. Sheng, L. Shao, J. J. Chen, W. J. Bao, F. B. Wang and X. H. Xia, *ACS Nano*, 2011, **5**, 4350–4358.
44 J. Liang, Y. Jiao, M. Jaroniec and S. Z. Qiao, *Angew. Chem., Int. Ed.*, 2012, **51**, 11496–11500.
45 Z. S. Wu, S. B. Yang, Y. Sun, K. Parvez, X. L. Feng and K. Müllen, *J. Am. Chem. Soc.*, 2012, **134**, 9082–9085.
46 T. N. Ye, L. B. Lv, X. H. Li, M. Xu and J. S. Chen, *Angew. Chem., Int. Ed.*, 2014, **53**, 6905–6909.
47 J. Jin, F. Pan, L. Jiang, X. Fu, A. Liang, Z. Wei, J. Zhang and G. Sun, *ACS Nano*, 2014, **8**, 3313–3321.
48 X. Wang, G. Sun, P. Routh, D. H. Kim, W. Huang and P. Chen, *Chem. Soc. Rev.*, 2014, **43**, 7067–7098.
49 X. Li, H. Wang, J. T. Robinson, H. Sanchez, G. Diankov and H. J. Dai, *J. Am. Chem. Soc.*, 2009, **131**, 15939–15944.
50 Y. J. Sa, C. Park, H. Y. Jeong, S. H. Park, Z. Lee, K. T. Kim, G. G. Park and S. H. Joo, *Angew. Chem., Int. Ed.*, 2014, **53**, 4102–4106.
51 H. Yin, C. Zhang, F. Liu and Y. Hou, *Adv. Funct. Mater.*, 2014, **24**, 2930–2937.
52 J. Sanetuntikul, T. Hang and S. Shanmugam, *Chem. Commun.*, 2014, **50**, 9473–9476.
53 J. Liang, R. F. Zhou, X. M. Chen, Y. H. Tang and S. Z. Qiao, *Adv. Mater.*, 2014, **26**, 6074–6079.
54 W. He, C. Jiang, J. Wang and L. Lu, *Angew. Chem., Int. Ed.*, 2014, **53**, 9503–9507.
55 W. Wei, H. W. Liang, K. Parvez, X. D. Zhuang, X. L. Feng and K. Müllen, *Angew. Chem., Int. Ed.*, 2014, **53**, 1570–1574.
56 Y. Zhao, C. G. Hu, L. Song, L. X. Wang, G. Q. Shi, L. M. Dai and L. T. Qu, *Energy Environ. Sci.*, 2014, **7**, 1913–1918.
57 K. Parvez, S. B. Yang, Y. Hernandez, A. Winter, A. Turchanin, X. L. Feng and K. Müllen, *ACS Nano*, 2012, **6**, 9541–9550.
58 D. Zhou, Y. Cui, P. W. Xiao, M. Y. Jiang and B. H. Han, *Nat. Commun.*, 2014, **5**, 4716, DOI: 10.1038/ncomms5716.